Check for updates

Engineering Transition Metal Layers for Long Lasting Anionic Redox in Layered Sodium Manganese Oxide

Natalia Voronina, Jun Ho Yu, Hee Jae Kim, Najma Yaqoob, Olivier Guillon, Hyungsub Kim, Min-Gi Jung, Hun-Gi Jung, Koji Yazawa, Hitoshi Yashiro, Payam Kaghazchi,* and Seung-Taek Myung*

Oxygen-redox-based-layered cathode materials are of great importance in realizing high-energy-density sodium-ion batteries (SIBs) that can satisfy the demands of next-generation energy storage technologies. However, Mn-based-layered materials (P2-type Na-poor $Na_y[A_xMn_{1-x}]O_2$, where A = alkali ions) still suffer from poor reversibility during oxygen-redox reactions and low conductivity. In this work, the dual Li and Co replacement is investigated in P2-type-layered Na_xMnO_2. Experimentally and theoretically, it is demonstrated that the efficacy of the dual Li and Co replacement in $Na_{0.6}[Li_{0.15}Co_{0.15}Mn_{0.7}]O_2$ is that it improves the structural and cycling stability despite the reversible Li migration from the transition metal layer during de-/sodiation. Operando X-ray diffraction and ex situ neutron diffraction analysis prove that the material maintains a P2-type structure during the entire range of Na^+ extraction and insertion with a small volume change of ≈4.3%. In $Na_{0.6}[Li_{0.15}Co_{0.15}Mn_{0.7}]O_2$, the reversible electrochemical activity of Co^{3+}/Co^{4+}, Mn^{3+}/Mn^{4+}, and $O^{2-}/(O_2)^{n-}$ redox is identified as a reliable mechanism for the remarkable stable electrochemical performance. From a broader perspective, this study highlights a possible design roadmap for developing cathode materials with optimized cationic and anionic activities and excellent structural stabilities for SIBs.

1. Introduction

Sodium-ion batteries (SIBs) are the most promising replacement for ubiquitous lithium-ion batteries (LIBs) owing to the lower price and availability of sodium salts, for which the resources are unlimited.[1,2] In particular, there has been a great increase in the demand for LIBs for powering electric vehicles and energy storage systems as inexpensive alternatives with an accessible base of needed raw materials.[3] The similarity of the basic principles of operation of SIBs and LIBs makes it possible to use existing production lines. Moreover, a great merit of SIBs is the possibility of using more environmentally friendly materials for anode materials such as hard carbon, which can be obtained from biomass.[4,5] Also, titanium-based anode materials such as oxides, phosphates, and MXene-based heterostructures are applicable due to ability of storage sodium ions.[6–8]

For the cathode side, materials for SIBs have an analogy with materials for LIBs, including the most popular types such as layered metal oxides and polyanionic compounds. Among these materials, layered Na_xMnO_2 has been particularly widely studied because of its high capacity, ease of synthesis, and low toxicity as well as the abundance of Mn. Na_xMnO_2 can be classified into two types depending on the sodium content: P-type (prismatic; P2 or P3

N. Voronina, J. H. Yu, H. J. Kim, S.-T. Myung
Hybrid Materials Research Center
Department of Nano Technology and Advanced Materials Engineering
Sejong Battery Institute
Sejong University
Seoul 05006, South Korea
E-mail: smyung@sejong.ac.kr

N. Yaqoob, O. Guillon, P. Kaghazchi
Forschungszentrum Jülich GmbH
Institute of Energy and Climate Research
Materials Synthesis and Processing (IEK-1)
52425 Jülich, Germany
E-mail: p.kaghazchi@fz-juelich.de

N. Yaqoob, P. Kaghazchi
MESA+ Institute for Nanotechnology
University of Twente
7500 AE Enschede, The Netherlands

H. Kim
Neutron Science Division
Korea Atomic Energy Research Institute (KAERI)
111 Daedeok-daero 989 Beon-Gil, Yuseong-gu
Daejeon 34057, South Korea

M.-G. Jung, H.-G. Jung
Center for Energy Storage Research
Korea Institute of Science and Technology
Seoul 02792, South Korea

K. Yazawa
Jeol Resonance Inc.
3-1-2 Musashino, Akishima, Tokyo 196–8558, Japan

H. Yashiro
Department of Chemical Engineering
Iwate University
Iwate 020–8551, Japan

for $x \leq 0.7$) or O-type (octahedral; O3 for $0.7 \leq x \leq 1$).[9] P2-type cathode materials generally exhibit higher capacity and better rate performance than O3-type cathode materials because of the large diffusion pathways, which enable higher Na$^+$-ion mobility than that of O3-type cathode materials.[10–13] Delmas et al.[9] first reported P2-type Na$_{0.7}$MnO$_2$ activated by the Mn^{4+}/Mn^{3+} redox pair; however, phase transitions such as P2–O2 on charge and P2–P'2 associated with the Jahn–Teller effect on discharge were not likely favored for retention of the capacity during cycling. To resolve these limits of Mn-based materials, the substitution of high spin Mn^{3+} ($t_{2g}^3 e_g^1$) with various transition metal elements (TM: Ni,[14,15] Fe,[16,17] Cu,[18] Co[19]) has been investigated. Dahn et al.[14] reported P2-Na$_{2/3}$[Ni$_{1/3}$Mn$_{2/3}$]O$_2$ with high capacity (173 mAh g^{-1}) and high operating voltage over 3.5 V in Na cells. However, the cyclability suffered as a result of the P2–O2 phase transformation, resulting in ≈23% volume change in unit cells in the highly desodiated state. Later, Konarov et al.[15] reduced the volume change to ≈13% by optimizing the Ni content in Na$_{2/3}$[Ni$_{0.2}$Mn$_{0.8}$]O$_2$, showing an acceptable level of capacity retention. Compared with P2-Na$_{0.7}$MnO$_2$, the suppression of Jahn–Teller distortion via Ni^{2+} incorporation is also worth mentioning as an approach to retain the capacity. Yabuuchi and Komaba et al.[16] stabilized the P2 layered structure by replacing half of the Mn^{3+} with Fe^{3+}, P2-Na$_{2/3}$[Fe$_{1/2}$Mn$_{1/2}$]O$_2$, which delivered a capacity of 190 mAh g^{-1} with good reversibility assisted by both Mn^{4+}/Mn^{3+} and Fe^{4+}/Fe^{3+} redox pairs. Different from the above works, desodiation of Na$_{2/3}$[Fe$_{1/2}$Mn$_{1/2}$]O$_2$ induced the formation of the OP4 phase in the highly desodiated state. Bruce et al.[17] investigated Ni, Fe-co-doped Na$_{2/3}$[Ni$_{1/6}$Mn$_{1/2}$Fe$_{1/3}$]O$_2$ that successfully diminished the P2–O2 phase transition above 4.1 V. In addition, they observed the so-called "Z"-phase, namely, an intergrowth structure between the P2 and O2 phases (OP4). According to their results, the formation of the "Z"-phase, which undergoes less volume change without abrupt structure change compared with the O2 phase, is beneficial for capacity retention, as observed in Yabuuchi and Komaba's work.[16] In an attempt to improve the electrode performance at high rates, Kang et al.[18] introduced Cu^{2+} in P2-Na$_{0.67}$[Cu$_x$Mn$_{1-x}$]O$_2$. Although the capacity decreased to a certain extent, the resulting operation voltage was increased because of the Cu^{3+}/Cu^{2+} redox pair. The inherent high electroconducting character of Cu contributed to the cell operation at 12 C. Konarov et al.[19] also introduced Co^{3+} into P2-Na$_{2/3}$MnO$_2$ to dilute the Jahn–Teller effect over Mn^{3+}O$_6$ octahedra, showing good electrode performance. The above works highlight the importance of substituents to stabilize the structure from the existing Jahn–Teller effect in Mn^{3+}O$_6$ octahedra in a deeply discharged state and suppression of volume change in unit cells during repetitive de/sodiation.

The increase in capacity can be achieved not only by doping electroactive TMs (Ni, Fe, Cu, and Co) in Na$_x$MnO$_2$ but also by using electro-inactive doping, such as Li,[20–22] Mg,[23–25] and Zn[26,27] or even vacancies □.[28,29] This type of doping leads to the Na–O–A configuration (A = Li, Mg, Zn, □) and causes the formation of oxygen lone-pair states, which activates oxygen-redox reactions. The capacity in binary P2-Na$_x$[A$_y$Mn$_{1-y}$]O$_2$ (A = Li, Mg, Zn, □) systems is delivered by Mn redox and oxygen redox. However, most of these binary systems with A = Li, Mg, and Zn suffer from low operation voltage and large

voltage hysteresis between charge and discharge.[20–27] A survey of the literature reveals that it may be related to Li migration from the TM to Na layer and the rearrangement of Mn in the TM layer.[22] For example, Bruce et al.[22] showed that the in-plane Li/Mn rearrangement in Na$_x$[Li$_y$Mn$_{1-y}$]O$_2$ materials can be reduced by the formation of a Li/Mn ribbon superstructure with less in-plane reordering than in the Li/Mn honeycomb superstructure. For Mg- and Zn-doped materials, high voltage hysteresis can also be associated with Mg and Zn migration and further rearrangement of Mn in the TM layer; however, there is no direct experimental evidence of such migration yet.[23–27] Interestingly, ternary systems of Li(Mg,Zn)/Ni(Co)/Mn in TM layers such as Na$_x$[Li$_{0.15}$Ni$_{0.15}$Mn$_{0.7}$]O$_2$,[20,30] Na$_x$[Mg$_{0.15}$Ni$_{0.15}$Mn$_{0.7}$]O$_2$,[31] Na$_x$[Zn$_{0.15}$Ni$_{0.15}$Mn$_{0.7}$]O$_2$,[32] Na$_{0.6}$[Mg$_{0.2}$Co$_{0.2}$Mn$_{0.6}$]O$_2$,[33] exhibit higher operation voltage, smaller voltage hysteresis, and better long-term cycling stability than binary systems. This may be related to the higher degree of Ni^{2+}/Ni^{4+} (Co^{3+}/Co^{4+}) participation and dilution of Jahn–Teller Mn^{3+}/Mn^{4+} domination together with a reduced degree of O^{2-}/(O$_2$)$^{n-}$ involvement. Most of these ternary compounds in TM layers typically undergo P2–OP4–P2 phase transformation (Li/Ni/Mn,[20] Mg/Ni/Mn,[31] Zn/Ni/Mn,[32] Mg/Co/Mn[33]) with relatively large volume change of ≈10% in the high desodiation state. Therefore, mitigation of structural changes by using different dopants and vacancies for the design of new P2-type materials with long-term stable cycling performance is urgently needed.

In this work, we investigate the effect of Li and Co co-doping on the crystal structure and electrochemical performance of P2-type Na$_x$MnO$_2$. It is anticipated that having Na–O–Li configuration in a Mn^{4+}-based layered material is important to active oxygen redox and that Co^{3+} is crucial for improving conductivity. Therefore, we, for the first time, developed a Na$_{0.6}$[Li$_{0.15}$Co$_{0.15}$Mn$_{0.7}$]O$_2$ (LCM) material with tetravalent Mn and a 1:1 ratio of Li:Co doping, for which the sodium level was adjusted to be 0.6 to compensate for the charge balance. This material crystallized into the P2-type layered structure with a random distribution of Li/Co/Mn cations in the TM layer. No phase transitions occurred upon Na$^+$ de/intercalation, as evidenced by *operando* X-ray diffraction (*o*-XRD) analysis. Moreover, X-ray absorption near edge structure (XANES) and electron spin resonance (EPR) spectroscopy revealed Co^{3+}/Co^{4+}, Mn^{3+}/Mn^{4+}, and O^{2-}/(O$_2$)$^{n-}$ redox-pair participation. Through ^{7}Li nuclear magnetic resonance (NMR, 2D pj – magic-angle turning and phase-adjusted sideband separation (MATPASS) pulse sequence), neutron diffraction (ND), and density functional theory (DFT) calculation, we reveal that Li$^+$ migration was partially reversible. Our findings indicate that the migration of the Li element is the trigger for a stable oxygen-redox reaction and structural stabilization of the material in general; in addition, Co substitution promotes improved capacity retention and kinetic properties of the material.

2. Results and Discussion

Figure 1a,b presents XRD and ND patterns of the as-synthesized P2-type Na0.6[Li0.15Co0.15Mn0.7]O2 powder, respectively, with both refined using the hexagonal P63/mmc space group.
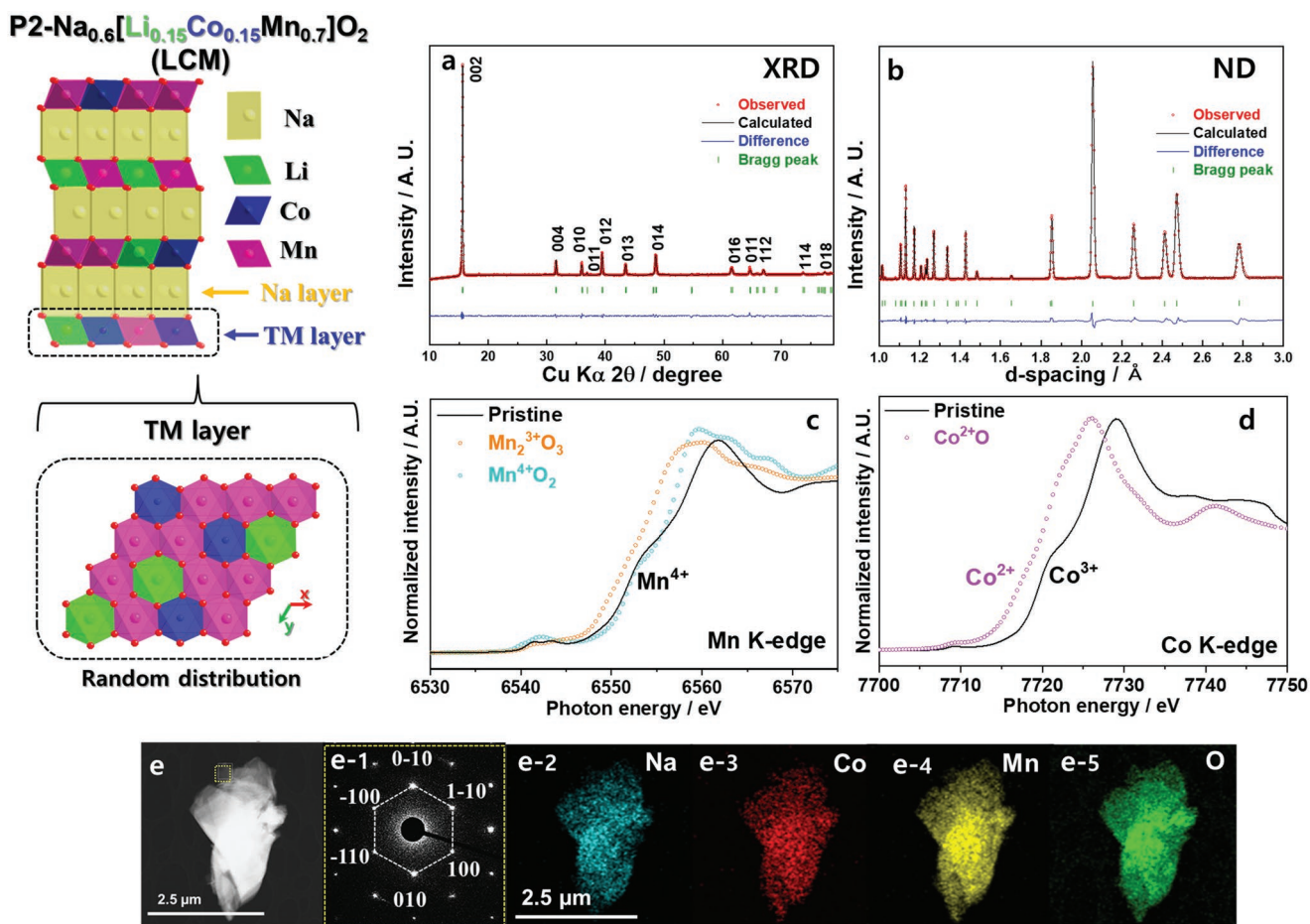
Figure 1. Schematic illustration of LCM crystal structure. Rietveld refinement of powder a) XRD and b) ND patterns for Na0.6[Li0.15Co0.15Mn0.7]O2. XANES spectra of c) Mn K-edge and d) Co K-edge of LCM compound. e) HRTEM image of LCM material with corresponding e-1) SAED pattern along [001] zone axis and e-2–e-5) EDS mapping data for Na, Co, Mn, and O elements.

No additional superlattice diffraction peaks were observed in the range of 18°–30° for both the XRD and ND patterns, indicating the disordered character of the Li/Co/Mn arrangement in the TM layer. The lattice parameters and volumes for LCM, obtained from Rietveld refinement of the XRD and ND patterns, were similar, as shown in Tables S1 and S2 (Supporting Information), respectively. The resulting structure determined based on the refinement data is shown in the inset of Figure 1a,b. To confirm the average oxidation states of the transition metals, XANES analysis of LCM was performed (Figure 1c,d). The Mn k-edge spectra indicate that the average oxidation state of Mn is close to Mn4+ (Figure 1c). The photon energy of the Co k-edge of LCM shifted toward higher energy compared with that of CoO, indicating that the oxidation state of Co is close to Co3+ (Figure 1d). Both Co and Mn k-edge EXAFS spectra show two distinct peaks: the first peaks ≈1.4 Å for the nearest Co/Mn-O6 bond and the second peaks at ≈2.5 Å for the second nearest Co/Mn-Co/Mn/Li bond within the TM layers. In consideration of bond lengths Co-O (1.93 Å) and Co-Mn/Co/Li (2.85 Å) are slightly larger than Mn-O (1.89 Å) and Mn-Mn/Co/Li (2.79 Å) due to the difference in ionic radii between Co3+(0.545 Å) and Mn4+(0.53 Å). Moreover, the LCM material consisted of heterogeneous primary particles with sizes in the range of 1–3 µm (Figure S2, Supporting Information), and elemental mapping data clearly demonstrate that Na, Co, Mn, and O elements were uniformly distributed throughout the particle (Figure 1e; Figure S2, Supporting Information). The selected-area electron diffraction (SAED) pattern along the [001] zone axis indicates that the structure of LCM is highly crystalline and stabilized into the hexagonal symmetry (Figure 1e-1).

The electrochemical performance of LCM was evaluated in the voltage range of 1.5–4.6 V at a constant current of 26 mA g^{-1} (0.1C) (**Figure 2**; Figure S3, Supporting Information). The LCM electrodes delivered a first charge (oxidation) capacity of 130 mAh (g-oxide)$^{-1}$, which is consistent with ≈0.5 mol of Na$^+$ extraction per formula unit (f.u.) (Figure 2a). The LCM material exhibited a sloppy voltage profile in the voltage range of 2.75–4.25 V followed by a flat plateau at ≈4.3 V on first charge. The sloppy profile to 4.25 V is attributed to the negation of Na$^+$/vacancy ordering suppressed by Li and Co replacement in the TM layer compared with that in Na$_{0.67}$MnO$_2$ (Figure S3b,d, Supporting Information). The long, flat voltage plateau appearing at ≈4.3 V is associated with a reaction other than Co and Mn redox. As shown in Figure 1c, Mn has an average oxidation state of Mn^{4+}, such that further oxidation is not available in the tested voltage range. In addition, according to our
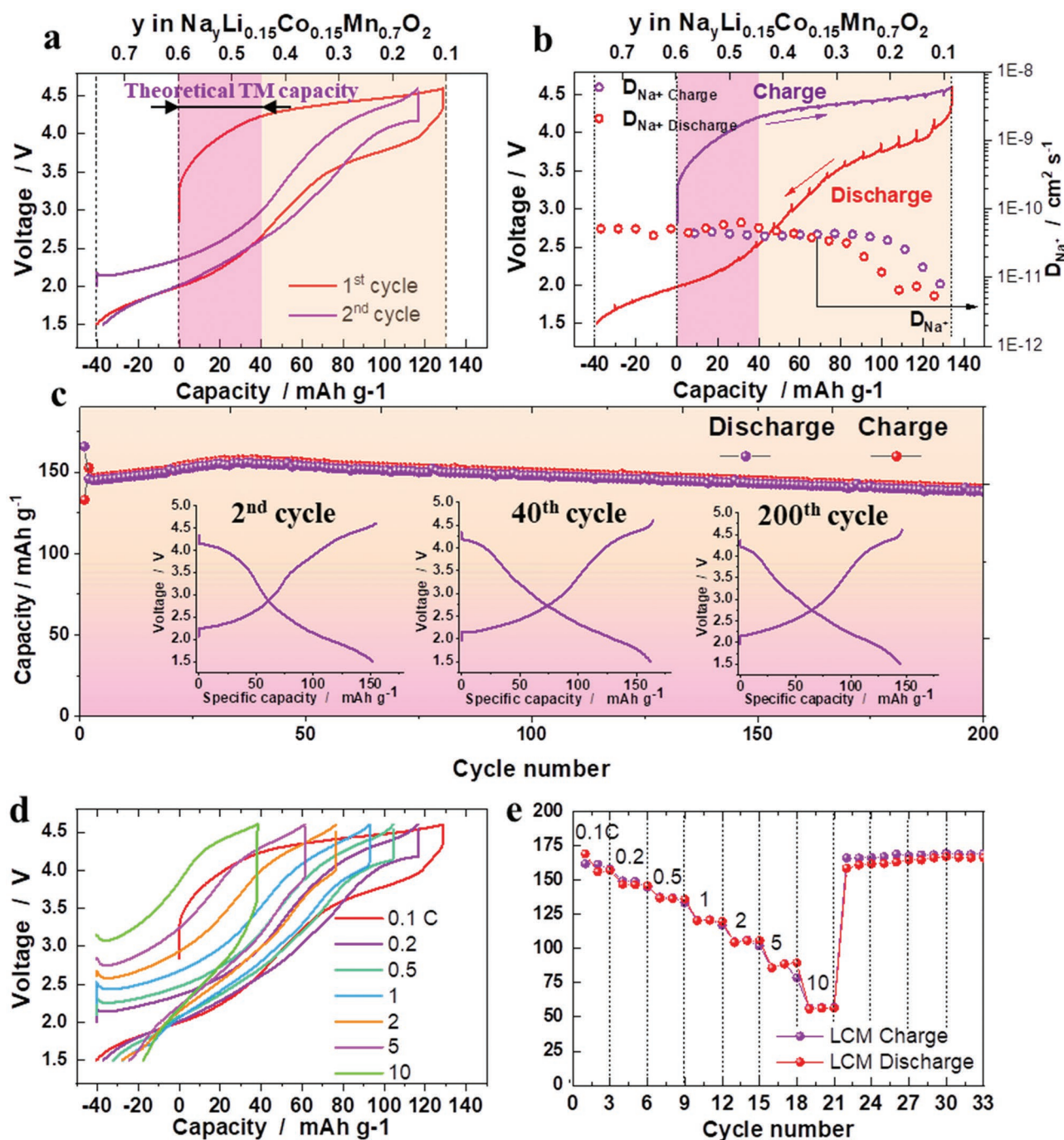
Figure 2. a) The first and second charge–discharge curves of LCM measured at a current of 26 mA g^{-1} (0.1 C) in the voltage range of 1.5–4.6 V at 25 °C. b) GITT curves and calculated D_{Na+} diffusion coefficient of LCM. c) Cyclability and selected charge/discharge curves of LCM at 0.1 C. d) Rate capability curves of LCM at different rates (0.1–10 C) and (e) the resulting plots of capacity versus currents.

earlier work,[19] the oxidation of Co^{3+} to Co^{4+} is limited to 4.2 V in Na cells, and the introduced Co content is only 15% in the TM layer; hence, the contribution of Co activity is not likely possible over 4.3 V. For this reason, it is suggested that the related activity would result from the possibility of oxygen-redox participation (O^{2-} to (O$_2$)$^{n-}$) over 4.3 V. The first discharge capacity of LCM was as large as 175 mAh g^{-1}, which is attributed to 0.75 mol of Na$^+$ insertion per f.u. On the first discharge,

the LCM material displays three sloppy plateaus centered at ≈4.3, ≈4.0, and ≈2 V. (Figure 2a). Similar to the charge curve, the Na$^+$/vacancy ordering was not evident during discharge (Figure 2a). It is also notable that the LCM electrode presents greatly reduced voltage hysteresis compared with P2-Na$_{2/3}$MnO$_2$ and P2-Na$_{0.67}$[Li$_{0.22}$Mn$_{0.78}$]O$_2$ electrodes (Figure S3b–d, Supporting Information). Compared with the P2-Na$_{0.67}$[Li$_{0.22}$Mn$_{0.78}$]O$_2$, the LCM electrode demonstrates less degree of O^{2-}/(O$_2$)$^{n-}$

participation and higher electrical conductivity, which would be possible reasons for the reduced voltage hysteresis after the first cycle. The calculated diffusion coefficients, which were measured by galvanostatic intermittent titration technique (GITT), can be divided into two regions; namely, the low-voltage region (1.5–3.5 V, $\approx 10^{-11}$ cm^{-2} s^{-1}) with a diffusivity one order higher than that for the high-voltage region (3.5–4.6 V, $\approx 10^{-12}$ cm^{-2} s^{-1}) in Figure 2b. The better kinetics result from the charge transfer by TM redox (Co^{3+}/Co^{4+} and Mn^{3+}/Mn^{4+}), which is typically faster than that by oxygen redox (O^{2-}/(O$_2$)$^{n-}$) that may contribute to the capacity at high voltage. Figure 2c shows the cyclability of the LCM electrode at 0.1C, with a capacity retention of $\approx 84\%$ after 200 cycles. As cycling progressed, the length of the plateau at ≈ 4.0 V on discharge was reduced. This is one of the possible reasons affecting the gradual capacity fade during cycling. The rate capability was also evaluated at various currents ranging from 0.1 C (26 mA g^{-1}) to 10 C (2600 mA g^{-1}) (Figure 2d), delivering a capacity of 147, 137, 120, 104, 85, and 55 mAh g^{-1} at 0.2, 0.5, 1, 2, 5, and 10 C, respectively. The recovered capacity at 0.1 C after the rate test reached $\approx 98\%$ (166 mAh g^{-1}) of the capacity obtained at the second discharge at 0.1 C. Compared with P2-Na$_{2/3}$MnO$_2$ and P2-Na$_{0.67}$[Li$_{0.22}$Mn$_{0.78}$]O$_2$ electrodes, the present LCM electrode exhibited better capacity for cycling (Figure S3e, Supporting Information), even at high rates (Figure S3f, Supporting Information). This finding implies that the dual introduction of Li and Co into P2-Na$_{0.6}$[Li$_{0.15}$Co$_{0.15}$Mn$_{0.7}$]O$_2$ enables significant improvement of the capacity retention and capacity at high rates, which may result from the increased conductivity of the materials and structural stability promoted by the dual replacement by Li and Co. The observed conductivity from the four-probe method was $\approx 5 \times 10^{-5}$ S cm^{-1} for P2-Na$_{0.6}$[Li$_{0.15}$Co$_{0.15}$Mn$_{0.7}$]O$_2$, which was higher than the values of $\approx 6 \times 10^{-6}$ S cm^{-1} for P2-Na$_{0.67}$MnO$_2$[15] and $\approx 5 \times 10^{-7}$ S cm^{-1} for P2-Na$_{0.67}$[Li$_{0.22}$Mn$_{0.78}$]O$_2$.[20] This improvement stems from the presence of Co^{3+} in the structure, as the overlapping in the density of states (DOS) between the O2p and Co3d (Co$^{4+/3+}$) orbitals enables facile electron transfer in P2-Na$_{0.6}$[Mg$_{0.2}$Co$_{0.2}$Mn$_{0.6}$]O$_2$.[33] Yabuuchi et al.[34] and de la Llave et al.[35] introduced Li substitution at the Mn site in P2-Na$_{5/6}$[Li$_{1/4}$Mn$_{3/4}$]O$_2$ and P2-Na$_{0.6}$[Li$_{0.2}$Mn$_{0.8}$]O$_2$, respectively, of which the Li in the TM layers played an important role in improving the structural stability compared with that of P2-Na$_{0.6}$MnO$_2$. Summarizing the above works, it is thought that the efficacy of dual Li and Co substitution resulted in improvement of the electrode performance supported by enhancement of electron transfer by Co and structural stability resulting from the presence of Li in P2-Na$_{0.6}$[Li$_{0.15}$Co$_{0.15}$Mn$_{0.7}$]O$_2$.

The structural evolution of the LCM electrode was investigated using *operando* XRD (*o*-XRD) as a function of Na content during the first two cycles in the voltage range of 1.5–4.6 V (**Figure 3**a,b). For the starting state, $x = 0.6$ in Na$_x$[Li$_{0.15}$Co$_{0.15}$Mn$_{0.7}$]O$_2$, the XRD pattern revealed the presence of the P2 layered structure, characterized by the (002)$_{P2}$, (004)$_{P2}$, (100)$_{P2}$, and (102)$_{P2}$ peaks at 15.9°, 32.2°, 36.5°, and 40.0° (2θ), respectively. Desodiation resulted in the (002)$_{P2}$ and (004)$_{P2}$ peaks shifting to lower angles in the range of $0.4 \leq x \leq 0.6$ in Na$_x$[Li$_{0.15}$Co$_{0.15}$Mn$_{0.7}$]O$_2$, whereas the (100)$_{P2}$ and (102)$_{P2}$ peaks shifted to higher angles. A continuous decrease of the a-lattice parameter was observed in this range, presumably due to the

oxidation of the TM elements, which spontaneously increases the repulsion in interslabs, thereby elongating the c-axis parameter (Figure 3c). Because of the inactive character of Mn^{4+}, Co is the only species that participates in the charge compensation process in the range of $0.4 \leq x \leq 0.6$ in Na$_x$[Li$_{0.15}$Co$_{0.15}$Mn$_{0.7}$]O$_2$. For $x \leq 0.4$ in Na$_x$[Li$_{0.15}$Co$_{0.15}$Mn$_{0.7}$]O$_2$, however, the delithiation resulted in a further shift of the XRD peaks ((002)$_{P2}$, (004)$_{P2}$, (100)$_{P2}$, and (102)$_{P2}$) toward higher angles, which induces contraction of both the a- and c-axes (Figure 3c). This tendency leads to a decrease of the metal–oxygen distance and increase in the covalency in the highly desodiated state. Note that the P2 phase did not change to the O2 or OP4 phase. The P2 phase remained intense in the highly desodiated state, in contrast to
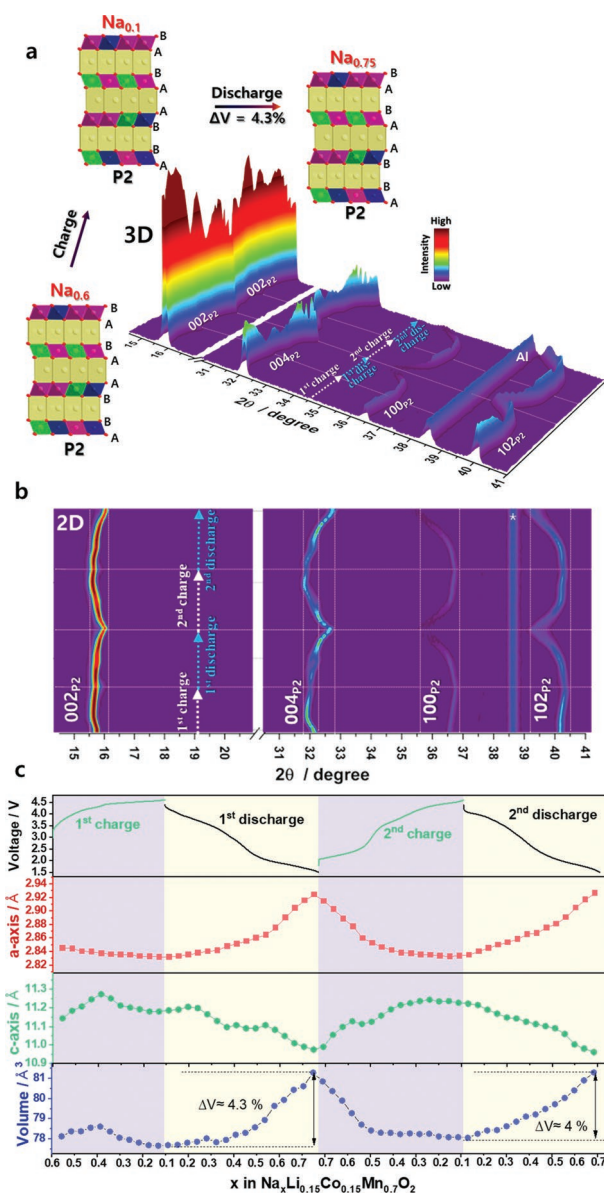

Figure 3. Structural evolution of LCM: a) 3D and b) 2D images of operando XRD data during the first two cycles and schematic illustration of structural evolution; c) the corresponding a- and c-axis parameters, and unit cell volume variations calculated from the operando XRD results.

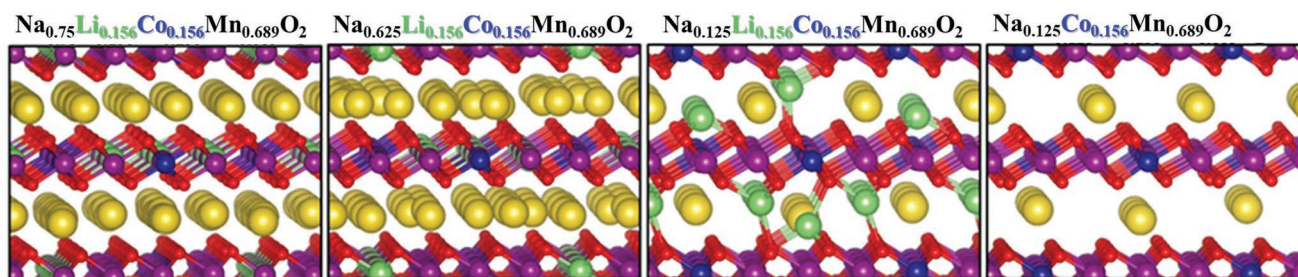**Figure 4.** Calculated atomistic structures of P2-Na$_x$Li$_{0.156}$Co$_{0.156}$Mn$_{0.689}$O$_2$ and P2-Na$_{0.125}$Co$_{0.156}$Mn$_{0.689}$O$_2$ using DFT-PBE+U. Na, Li, Co, Mn, and O are in yellow, green, blue, purple and red, respectively.

other P2 layered materials with oxygen redox such as Li-doped Na$_x$[Li$_y$Mn$_{1-y}$]O$_2$.[20,35] During sodiation (reduction) in the range of $0.1 \leq x \leq 0.75$ in Na$_x$[Li$_{0.15}$Co$_{0.15}$Mn$_{0.7}$]O$_2$, the (002)$_{P2}$, (004)$_{P2}$, (100)$_{P2}$, and (102)$_{P2}$ peaks recovered their positions in the pristine P2 phase (Figure 3a,b). The original P2 phase was retained throughout the sodiation, with no emergence of a new phase at the end of discharge. In summary, a single-phase reaction was observed for the LCM electrode within the entire operation window of 1.5–4.6 V. Because of small variations in the a- and c–axis parameters within the P2 phase, the resulting volume change was limited to ≈4.3% (Figure 3c). The monotonous single-phase reaction was continued within the P2 phase for the second cycle, which may be responsible for the capacity retention for 200 cycles. The above findings suggest that the dual Li and Co replacement in P2-Na$_{0.6}$[Li$_{0.15}$Co$_{0.15}$Mn$_{0.7}$]O$_2$ substantializes not only the improvement of the facile electron transfer assisted by the presence of Co but also stabilization of the structure by Li in the TM layers.

Using density functional theory (DFT) calculation, we simulated the effect of Li and Co doping on P2-Na$_x$MnO$_2$. The atomistic structures of P2-Na$_{0.75}$Li$_{0.156}$Co$_{0.156}$Mn$_{0.689}$O$_2$, P2-Na$_{0.625}$Li$_{0.156}$Co$_{0.156}$Mn$_{0.689}$O$_2$, P2-Na$_{0.125}$Li$_{0.156}$Co$_{0.156}$Mn$_{0.689}$O$_2$, and P2-Na$_{0.125}$Co$_{0.156}$Mn$_{0.689}$O$_2$ were determined by performing an extensive set of Coulomb energy calculations (**Figure 4**). The computed lattice parameters with DFT-PBE+U indicate that the a-axis parameter decreases from 2.96 to 2.92 Å, whereas the c-axis one increases from 11.01 to 11.15 Å when $x = 0.75 \rightarrow 0.625$. The decrease in the a-axis after desodiation is most likely due to the oxidation of Mn cations. The expansion of the c-axis is because of weakening of the electrostatic attraction between Na and O–TM–O layers with the extraction of Na ions. This trend agrees with our o-XRD measurement (Figure 3). With further desodiation of $x = 0.625 \rightarrow 0.125$ (**Table 1**), the computed lattice parameters indicate a small decrease in the a-axis parameter (from 2.92 to 2.89 Å) and relatively large decrease in the

c-axis parameter (from 11.15 to 10.70 Å). The decrease in the a-axis stems from the oxidation of the TM. However, the computed decrease in the c-value originates from the spontaneous migration of Li ions from TM to Na sites during geometry optimization. The computed contraction of c agrees well with our experimental data for the first charge (Figure 3c). To find whether the migrated Li ions from TM sites to Na sites move to the cathode surface or stay at Na sites after charge, we removed the Li ions from the Na sites in the charged system (modelled by P2-Na$_{0.125}$Co$_{0.156}$Mn$_{0.689}$O$_2$) and optimized the lattice parameters. It is found that the c-axis value expands from 10.70 to 11.42 Å, which agrees with our XRD data (Figure 3c). This result shows that no Li ions stay in the Na sites, which agrees with ^{7}Li NMR data, which will be discussed later. Therefore, we propose that the desodiation-induced expansion of the c-value for the charge would be due to the weakening of the electrostatic attraction between Na and O–TM–O layers because of the extraction of Na ions.

To study the redox mechanism, we computed the number of unpaired electrons (N_{unp}) on elements as well as the spin density differences (SDD) using DFT-HSE06. For Na$_{0.75}$[Li$_{0.156}$Co$_{0.156}$Mn$_{0.689}$]O$_2$ (modeled by Na$_{24}$Co$_5$Li$_5$Mn$_{22}$O$_{64}$), the calculated average values of N_{unp} ($\overline{N_{unp}}$) on Mn and Co cations were 3.19 and 0.04, indicating a charge state of 3.81+ and 3+, respectively, on these cations (**Figure 5** and **Table 2**). The desodiation-induced oxidation of each ion was then estimated by analyzing the change in its N_{unp} with desodiation. Ions with ΔN_{unp} values smaller than 0.05 were considered to preserve their charges. Upon a slight desodiation of $x = 0.75 \rightarrow 0.625$, the calculated $\overline{N_{unp}}$ of Mn becomes 3.06, indicating that Mn cations experience a slight oxidation from 3.81+ to 3.94+, whereas Co and O remain in their initial charge states, as clearly observed in the calculated N_{unp} (Table 2) and SDD plot (**Figure 6**). To study the redox mechanism for the charge/discharge endpoints, we focused on the desodiation of $x = 0.75 \rightarrow 0.125$

Table 1. Calculated lattice parameters of P2-Na$_x$Li$_{0.156}$Co$_{0.156}$Mn$_{0.689}$O$_2$ and P2-Na$_{0.125}$Co$_{0.156}$Mn$_{0.689}$O$_2$ using DFT-PBE and DFT-PBE+U with U(Co) = 5.9 eV, U(Mn) = 5.2 eV.

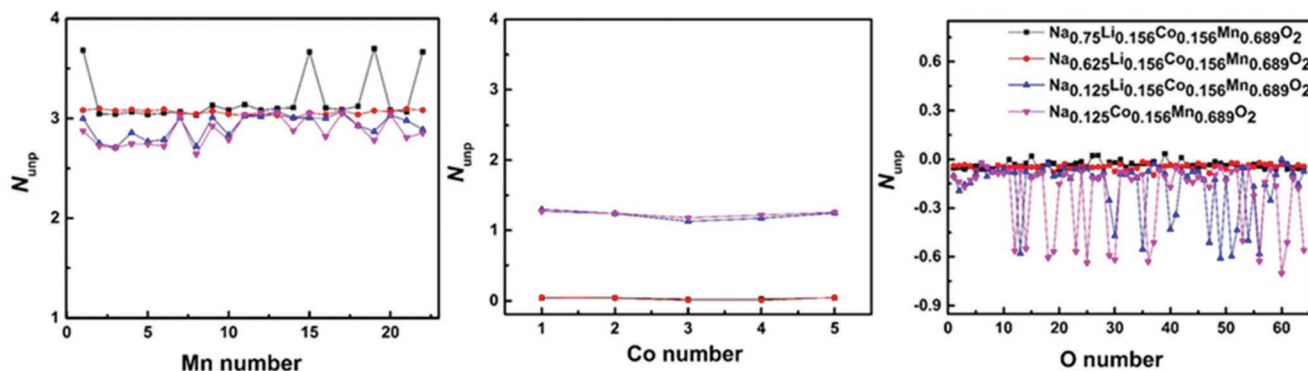| System	PBE		PBE+U	
	a	c	a	c
P2-Na$_{0.75}$Li$_{0.156}$Co$_{0.156}$Mn$_{0.689}$O$_2$	2.88	10.93	2.96	11.01
P2-Na$_{0.625}$Li$_{0.156}$Co$_{0.156}$Mn$_{0.689}$O$_2$	2.87	11.10	2.92	11.15
P2-Na$_{0.125}$Li$_{0.156}$Co$_{0.156}$Mn$_{0.689}$O$_2$	2.85	10.79	2.89	10.70
P2-Na$_{0.125}$Co$_{0.156}$Mn$_{0.689}$O$_2$	2.84	11.19	2.89	11.42

Figure 5. Computed number of unpaired electrons N_{unp} on Co and Mn cations as well as O anions for P2-$Na_xLi_{0.156}Co_{0.156}Mn_{0.689}O_2$ and P2-$Na_{0.125}Co_{0.156}Mn_{0.689}O_2$ with DFT-HSE06.

and considered two models for the low Na concentration: i) $Na_{0.125}[Li_{0.156}Co_{0.156}Mn_{0.689}]O_2$ and ii) $Na_{0.125}[Co_{0.156}Mn_{0.689}]O_2$. For $Na_{0.75}[Li_{0.156}Co_{0.156}Mn_{0.689}]O_2 \rightarrow Na_{0.125}[Li_{0.156}Co_{0.156}Mn_{0.689}]O_2$, the computed $\overline{N_{unp}}$ of Co cations is 1.22, indicating that each Co experiences an average oxidation of 0.78+ (considering a spin transition). The Mn cations experience an average oxidation of 0.27+. The clear increase in $\overline{N_{unp}}$ (Figure 5 and Table 2) and larger SDD (more blue features) of the oxygen anions (Figure 6) indicates their oxidation. The contribution of O anions to the redox process is estimated to be ≈50%. In total, 10 oxygen anions per unit cell ($O_{0.31}$) undergo a total oxidation of 5.28+ (an average oxidation of $\Delta q = 0.53+$), and 48 oxygen anions ($O_{1.5}$) experience a total oxidation of 4.88+ ($\Delta q = 0.10+$). The total desodiation-induced oxidation of oxygen is then calculated to be 0.31+ per formula unit. The contribution of TM redox is estimated to be 50%. 5Co ($Co_{0.16}$) and 22Mn ($Mn_{0.69}$) per unit cell undergo, respectively, a total oxidation of 3.90+ ($\Delta q = 0.78+$) and 5.83+ ($\Delta q = 0.27+$). The total desodiation-induced oxidation of TMs is 0.31+ per formula unit. For $Na_{0.75}[Li_{0.156}Co_{0.156}Mn_{0.689}]O \rightarrow Na_{0.125}[Co_{0.156}Mn_{0.689}]O$, the computed $\overline{N_{unp}}$ for Co cations is 1.23, indicating that all of them experience a Δq of 0.77+ (considering a spin transition) with desodiation. Δq is computed to be 0.32+ for Mn cations. A clear increase in $\overline{N_{unp}}$ (Figure 5 and Table 2) and larger SDD (more blue features) of oxygen anions (Figure 6) that have lost their binding to removed Li ions indicate that they undergo a significant oxidation. Both $\overline{N_{unp}}$ and SDD indicate that the three O anions that are the nearest neighbors of each Li vacancy experience a large oxidation. Thus, 15 O anions per unit cell ($O_{0.47}$) are oxidized after removing 5 Li ions. The total oxidation of these O anions is ≈9+. This means that only a total oxidation of ≈4+ ($\Delta q = 0.27+$) is due to the desodiation, and the rest is induced by the extraction of 5 Li. The rest of the 49 O per unit cell ($O_{1.53}$) experience partial oxidations

with a total charge of ≈5+ ($\Delta q = 0.10+$). The total desodiation-induced oxidation of oxygen is then ≈0.28+ per formula unit. The contribution of oxygen to the total oxidation is estimated to be ≈45%. The rest is due to the oxidation of TMs, namely $Co_{0.16}^{0.77+}$ and $Mn_{0.69}^{0.32+}$.

To attain further insight into the charge-compensation process, we performed ex situ Mn-, Co-, and O- k-edge XANES measurements for Mn, Co, and O elements for the LCM electrodes at different states (fresh, fully charged, and fully discharged) (**Figure 7**). For the Mn k-edge spectra (Figure 7a), the corresponding chemical shift of the spectrum was negligible after charging to 4.6 V, meaning that Mn is stabilized as 4+ and inactive on charge. However, after discharging of the LCM electrode to 1.5 V, the Mn K-edge spectrum showed a chemical shift toward lower energy, indicating reduction of Mn toward 3+ while the average oxidation state reaches ≈$Mn^{3.78+}$ according to a linear fitting of the spectra. During the desodiation, the Co k-edge spectrum showed an obvious shift of the pre-edge (≈7709 eV, 1s→3d transition) and white beam (≈7729 eV, 1s→4p transition) peaks to higher energy positions (Figure 7b), because of oxidation of Co^{3+} toward Co^{4+}. Subsequent discharge to 1.5 V led to the reduction of Co^{4+} to Co^{3+}, indicating a reversible Co^{3+}/Co^{4+} redox in the voltage range of 1.5–4.6 V. As demonstrated on charge, the only Co^{3+}/Co^{4+} redox is responsible for the compensation process, theoretically delivering a capacity of ≈39 mAh g^{-1}. However, the LCM delivered a first charge capacity of 130 mAh g^{-1} (Figure 2a), for which the rest of the capacity was provided by the oxidation of oxygen $O^{2-}/(O_2)^{n-}$ (91 mAh g^{-1}). Thus, the O K-edge XANES spectra were measured in a total-fluorescence-yield (TFY) mode, of which the two pre-edge peaks appeared at ≈529.4 and 531.6 eV, corresponding to the TM3d–O2p t_{2g} and e_g hybridized states, respectively, for the fresh state (Figure 7c). After charging

Table 2. Calculated averaged number of unpaired electrons Nunp on cations and anions of P2-$Na_xLi_{0.156}Co_{0.156}Mn_{0.689}O_2$ as well as P2-$Na_{0.125}Co_{0.156}Mn_{0.689}O_2$ using the DFT-HSE06 functional.

System	Na	Li	Mn	Co	O
P2-$Na_{0.75}Li_{0.156}Co_{0.156}Mn_{0.689}O_2$	0.0	0.0	3.19	0.04	−0.03
P2-$Na_{0.625}Li_{0.156}Co_{0.156}Mn_{0.689}O_2$	0.0	0.0	3.06	0.03	−0.05
P2-$Na_{0.125}Li_{0.156}Co_{0.156}Mn_{0.689}O_2$	0.0	0.0	2.93	1.22	−0.17
P2-$Na_{0.125}Co_{0.156}Mn_{0.689}O_2$	0.0	–	2.88	1.23	−0.22
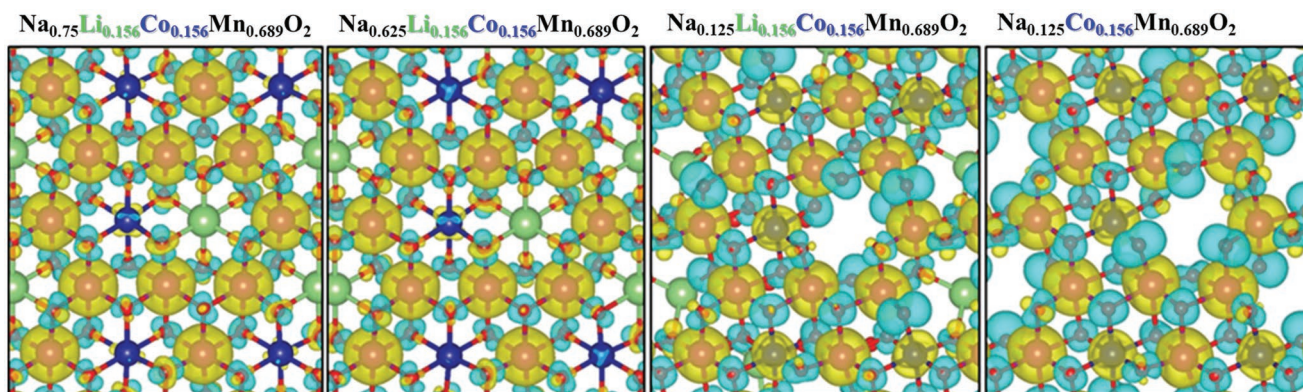
Figure 6. Calculated spin density difference (SDD) (with an isosurface of 0.006 eV Å^{-3}) for P2-Na$_x$Li$_{0.156}$Co$_{0.156}$Mn$_{0.689}$O$_2$ as well as P2-Na$_{0.125}$Co$_{0.156}$Mn$_{0.689}$O$_2$ with DFT-HSE06. Na, Li, Mn, Co, and O are in yellow, green, purple, blue, and red, respectively. The up- and down-spin electrons in the SDD plot are in yellow and blue, respectively.

to 4.6 V, the normalized intensity of the 531.6 eV peak was increased, corresponding to the absorption energy of oxidized species in the e_g orbital that indicates the formation of lone-pair electrons. In the discharge state, the spectrum overlapped with that of the fresh state, indicating the reduction of oxygen and reversible occurrence of oxygen redox.

The reversibility of the oxygen redox of the LCM material is further highlighted in the ex situ electron paramagnetic resonance (EPR) measurements performed at 5 K (Figure 7d). For the fresh LCM material, the Mn^{4+}–O signal appears as a broad symmetric signal centered at $g = 1.99$ in perpendicular mode.[36–38] Upon charging to 4.6 V, the EPR spectra of the LCM material contained an almost flatted paramagnetic Mn^{4+}–O signal (Figure 7d). This feature is related to the strong Co^{4+}–Mn^{4+} magnetic coupling[39] and oxidation of oxygen from O^{2-} to (O$_2$)$^{n-}$ because Mn^{4+} is unlikely to be oxidized in an octahedral environment, as expected previously by Hu et al.[28] Moreover, the six-fold Mn^{4+}–O hyperfine splitting, which is anisotropic, was observed in the fully charged state (Figure 7d inset). Huq et al.[28] reported that this feature can be attributed to the
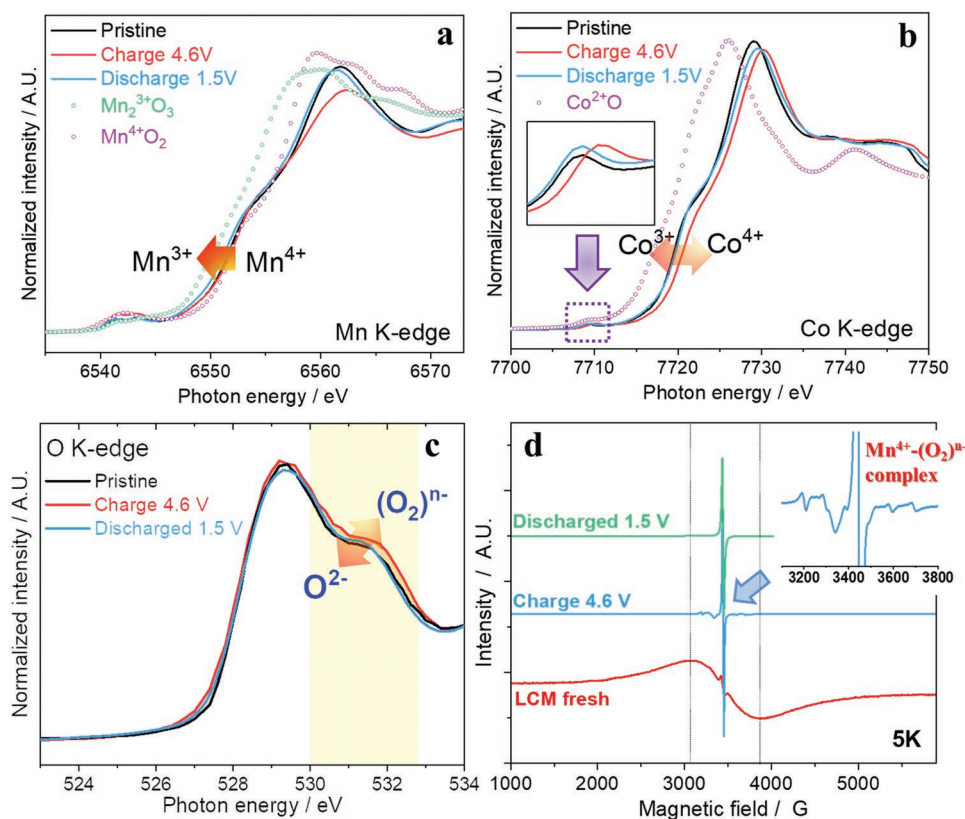

Figure 7. XANES spectra of a) Mn k-edge, b) Co k-edge, and c) O k-edge for LCM. d) Ex situ electron paramagnetic resonance spectroscopy at fresh, fully charged (4.6 V), and fully discharged (1.5 V) states.
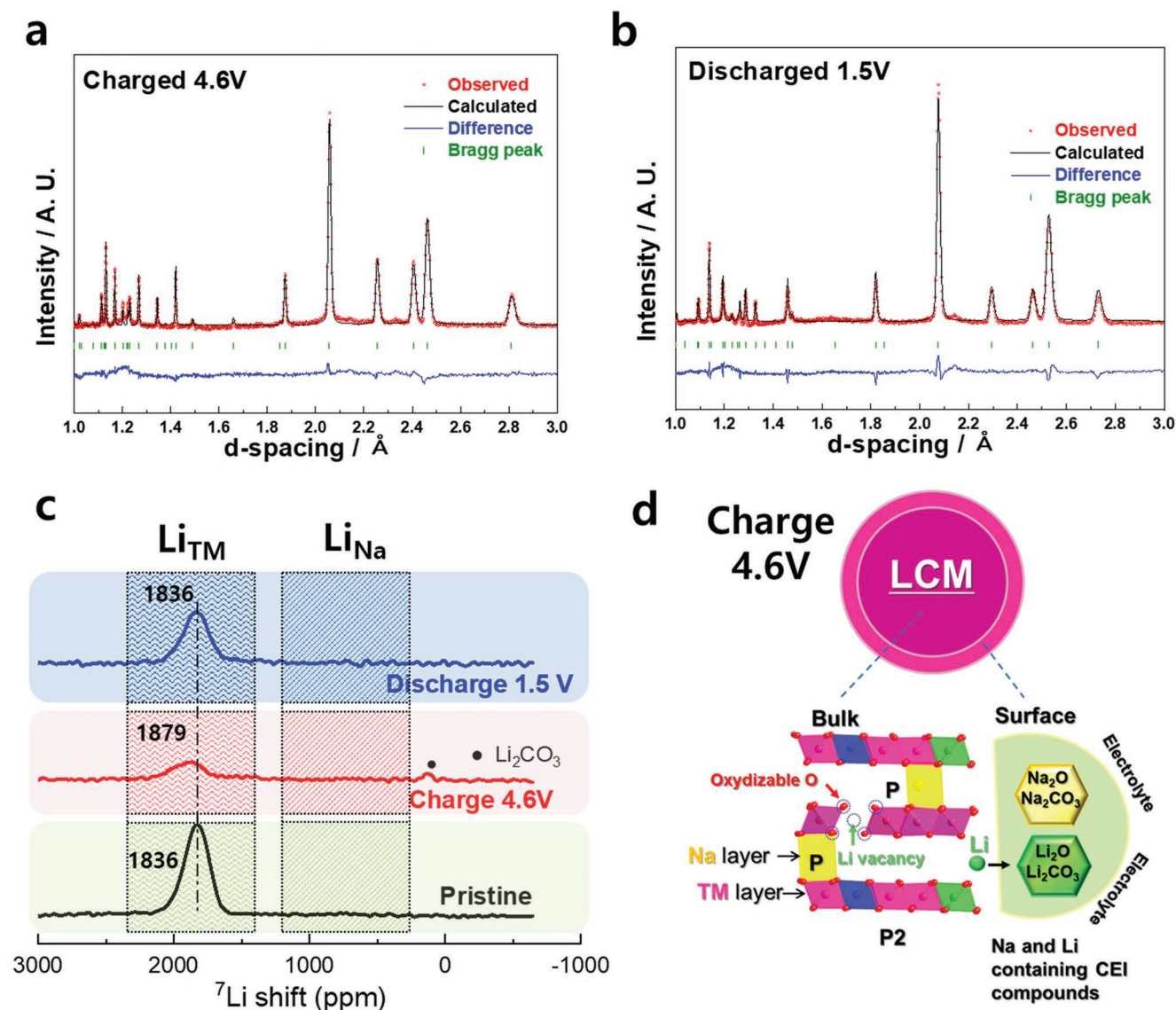
Figure 8. ND patterns for LCM electrodes a) charged to 4.6 V b) discharged to 1.5 V. c) 7Li ssNMR spectra with pj MATPASS pulse sequence for LCM materials. d) Structure and surface evolution in LCM material at charged state 4.6 V.

vacancy-mediated structure. After discharge to 1.5 V, the LCM material exhibited two features, namely, the disappearance of the hyperfine splitting and the offset of the broad symmetric signal of Mn^{4+} ($t^3_{2g}e^0_g$). Such a strikingly different spectrum compared with that of the fresh state can be explained by the reduction of Mn^{4+} toward Mn^{3+}, which quenches the Mn^{4+} signal in LCM toward Mn^{3+} ($t^3_{2g}e^1_g$).[37] From the above spectroscopic analyses, it is evident that the present LCM material undergoes a reversible charge-compensation process via Mn^{3+}/Mn^{4+}, Co^{3+}/Co^{4+}, and $O^{2-}/(O_2)^{n-}$ redox moieties in Na cells.

Further, ND, ^7Li NMR with MATPASS pulse sequence, ICP, and TOF-SIMS were used to investigate the role of Li^+ migration during Na^+ de-/intercalation in the LCM material (**Figure 8**). First, we evaluated the fractional occupancy of Li in *2a* octahedral TM sites using Rietveld refinements of ND patterns at fully charged (4.6 V) and fully discharged (1.5 V)

states (Figure 8a,b). Upon charge to 4.6 V, the structure of the LCM material remained the hexagonal P2 structure ($P6_3/mmc$ space group) with the decreased $a = 2.839$ Å lattice parameter, implying a decreased ionic radii of the Co and O ions with increasing valence state of Co^{3+} (0.545 Å) to Co^{4+} (0.53 Å) and O^{2-} (1.4 Å) to $(O_2)^{n-}$ (<1.4 Å). Moreover, we observed the Li tendency to be decreased, due to the extraction of Li from 0.15 to 0.05 in the *2a* octahedral TM site (Table S2, Supporting Information). Upon discharge, the LCM material still maintained its hexagonal P2 structure with increased $a = 2.916$ Å and decreased $c = 10.910$ Å lattice parameters, which are in good agreement with the o-XRD data (Figure 3c). Importantly, the increased occupancy of Li in the *2a* TM site was confirmed, with Li^+ reinserting into the octahedral site of the host LCM P2-structure (Table S2, Supporting Information).

To probe the local structure evolution around Li, ^7Li NMR measurements with pj MATPASS pulse sequence were

performed, as shown in Figure 8c. The ^{7}Li NMR spectra of the fresh LCM material showed distinct resonance centered at $\approx$1836 ppm, indicating the presence of Li element in the TM layer. At the end of charge (4.6 V), the intensity of this resonance was greatly reduced, and the peak shifted toward higher ppm values (centered at $\approx$1879 ppm). The lowered intensity is attributed to the reduced amount of Li in the TM layer, such that the position shift is provided by the local changes of the Li environment in the TM caused by oxidation of Co^{3+} to Co^{4+} and O^{2-} to $(O_2)^{n-}$. Moreover, there were no visible signals in the range of 200–1000 pm, indicating that Li^+ is not present in the Na layer after desodiation. It is hypothesized that because the interslab can be too large to accommodate Li^+ into the prismatic environment in the P2 phase, the desodiation did not induce new phases with an octahedral environment in the Na layer, as verified by o-XRD data (Figure 3a). This observation is further evidenced by the ICP-AES and TOF-SIMS results for desodiated and sodiated LCM electrodes (Figure S4, Tables S3 and S4, Supporting Information). According to the ICP-AES results, the Li content was greatly reduced after charging the LCM electrode to 4.6 V. Moreover, we analyzed the surface state of the charged electrode using TOF–SIMS. There were clear emergences of $LiCO_2^+$ ($m/z = 51.01$), Li_2O^+ ($m/z = 30.03$), $NaCO_2^+$ ($m/z = 66.98$), and Na_2O^+ ($m/z = 61.98$) fragments after charging the LCM electrode to 4.6 V, whereas those fragments were notably diminished after discharging to 1.5 V (Figure S4, Supporting Information). The formation of these fragments in TOF-SIMS is interpreted as the formation of Li_2CO_3, Li_2O, Na_2CO_3, and Na_2O compounds as the surface deposits. More interestingly, the relative intensity of the $LiCO_2^+$ and Li_2O^+ fragments appeared almost same as that of $NaCO_2^+$ and Na_2O^+ fragments on charge, implying that a large portion of Li^+ is present on the surface of the LCM electrode. Moreover, the ICP measurements of Li concentrations in electrolyte at charged and discharged states showed the presence of Li in electrolyte on charge and decrease of its concentration on discharge (Table S4, Supporting Information). On discharge to 1.5 V, the ^{7}Li NMR resonance at $\approx$1879 ppm was shifted back to the original position at $\approx$1836 ppm, and its intensity was partially restored (Figure 8c), suggesting that the Li ingredient returned to the original sites in the TM layers. This finding agrees with the ND data shown in Figure 8a,b.

To elucidate the reversibility of the oxygen-redox reaction and prove the absence of O_2 gas evolution, *operando* differential electrochemical mass spectrometry (*o*-DEMS) was employed (Figure S8, Supporting Information). For the LCM electrode, visible CO_2 gas evolution was detected throughout the entire charge process up to 4.6 V, with a subsequent moderate decrease during the discharge process. The CO_2 gas release generally originates from residual carbonates on the surface of the electrode that remain after synthesis (low-voltage release 3.0–4.4 V) and the electrolyte decomposition products (high-voltage release 4.4–4.6 V).[35,38] In addition, the evolution of O_2 gas was not detected from the LCM electrode (Figure S8, Supporting Information). These results validate the idea that direct oxygen loss did not occur from the lattice of the LCM electrodes, which may be an indication of reversible $O^{2-}/(O_2)^{n-}$.

The post-cycled LCM electrode was recovered from the coin cell after 200 cycles, and XRD and TEM were used to examine the structural stability (Figure S9, Supporting Information). The XRD spectra indicates that that LCM material maintained the original P2-type crystal structure with lattice parameters of $a = 2.87$ Å and $c = 11.05$ Å, which are close to the values of the pristine sample. However, the relative intensity decreased together with an increase in broadness of the XRD peaks, which may be the result of repetitive Li migration from the TM. Additionally, HRTEM analysis with SAED patterns along the [001] zone axis for the LCM materials confirmed the maintenance of the original P2 crystal structure.

Summarizing the above results of ND, 7Li NMR, ToF-SIMS, and ICP-AES, Na^+ de-/intercalation from LCM occurred along with partially reversible migration of Li^+ out of the LCM structure. Since the migrated Li did not suit the prismatic Na site, because the size of prismatic site is too large to properly accommodate the small Li^+ ions. Thus, there was no preference for Li^+ to be stabilized in Na layers in LCM, while it is more preferable for Li^+ to form surface deposits as a CEI layer on the surface and to be present in the electrolyte. The Li^+ migration creates vacancies in the TM layer, producing lone-pair electrons and promoting the oxygen-redox reaction at high voltage. The Li^+ migration is partially reversible, such gradual loss of Li ingredient to the CEI layer is likely to shorten the length of the voltage plateau on 4 V, affecting rise of cell impedance (Figure S5, Supporting Information) caused by the thickened CEI layer (Figures S6 and S7, Supporting Information) to result in gradual capacity fading (Figure 2c). To overcome those intrinsic shortcomings, further work is required to stabilize not only the structure through formation of ordering of alkali/TM element in the TM layer by dopings to adopt Li element in the Na layer when desodiated but also surface modification to stabilize the surface reaction.

As designated, the efficacy of the dual replacements resulted in structural integrity and improved conductivity, thereby improving the electrode performance. The voltage hysteresis between charge and discharge is a typical process of oxygen redox cathode materials. Indeed, there are few sodium cathodes that demonstrate low hysteresis on high voltage region, such as P2-$Na_{0.6}[Li_{0.2}Mn_{0.8}]O_2$[22] and $P\bar{1}$ – type $Na_2Mn_3O_7$[28] Those works demonstrated that the low hysteretic behavior is attributed to formation of robust structural framework for oxygen redox, with the ordering of alkali/TM in the TM layer, which prevents vacancy clustering and O_2 gas formation. For the present LCM cathode, there was no in-plane ordering of alkali/TM elements in the TM layer. Such random distribution of elements in the TM layer may cause such hysteresis for the first cycle. As we mentioned in ND and 7Li ssNMR spectra with pj MATPASS pulse sequence in Figure 8 and Tables S2–S4 (Supporting Information), Li^+ migration was partially reversible during the first cycle, leaving vacancies in the Li site of the TM layer. This structural reorganization would be associated with the reduced voltage hysteresis from the second cycle in Figure 2a. Similar behavior was also observed for oxygen redox P2-type cathodes for SIBs and Li-rich layered cathodes for LIBs, where staircase behavior on charge was transformed to S-shaped curves on discharge with reduced voltage hysteresis between charge and discharge. In comparison to LM material (Figure S3, Supporting Information), the current LCM cathode demonstrated less degree of $O^{2-}/(O_2)^{n-}$ participation and higher

electrical conductivity, which would be possible reasons for the reduced voltage hysteresis after the first cycle.

The observed behavior was different from earlier works in the literature, including ^{7}Li NMR studies of P2-type $Na_x[Li_yMn_{1-y}]O_2$ (LM)[20,36,37] and $Na_x[Li_{0.15}Ni_{0.15}Mn_{0.7}]O_2$ (LNM),[20,40] where reversible migration of the Li element was observed in Na layers in the desodiated state. This difference correlates well with the different phase transitions for LCM (solid-solution P2) compared with LM (P2–P2 with O stacking faults-P2/P'2) and LNM (P2–OP4–P2), as the stacking fault formation in the LM material and OP4 phase formation in LNM are due to the preference of Li$^+$ to be located in an octahedrally coordinated environment rather than prismatic surroundings in Na layers. The achieved structural integrity, with the P2 phase maintained during de-/sodiation, revealed that the dual Li and Co substitution in Na_xMnO_2 provides fairly reversible redox reactions induced by transition metals and oxygen, affecting the improved cycling and rate performance of $Na_{0.6}[Li_{0.15}Co_{0.15}Mn_{0.7}]O_2$ as a cathode for SIBs.

3. Conclusion

The purpose of the present work is not the record-breaking capacity, but elucidation of reaction mechanism by changing element in transition metal layer: migration of Li from TM to Na layers triggers oxygen redox, and Co provides electronic conductivity. So far as we know, this is the first report on Li and Co dual-substitution on structural and electrochemical stability and redox mechanism of P2-Na_xMnO_2 layered material. We investigated the effect of dual Li and Co substitution in P2-Na_xMnO_2 to suppress the large volume change in the high-voltage region during cycling and improve the cyclability of the material. The sodium storage mechanism was investigated using a combination of electrochemical techniques, operando XRD, ex situ XANES, and ^{7}Li NMR and EPR spectroscopies. The XANES and EPR techniques confirmed the participation of both Co^{3+}/Co^{4+}, Mn^{3+}/Mn^{4+}- cationic and O^{2-}/(O$_2$)$^{n-}$- anionic redox. The dual Li and Co substitutions enabled a full range of solid-solution behavior with a low volume change of 4.3%. The ^{7}Li NMR study confirmed the partial Li extraction from the TM with the preference of forming a CEI layer on the surface and of being present in the electrolyte. Moreover, the oxygen-redox reaction O^{2-}/(O$_2$)$^{n-}$ was reversible with no oxygen gas evolution, which allowed Li$^+$ to migrate reversibly into the TM layers. Therefore, our finding validates that the presence of Li and Co played important roles in the structural stability, thereby improving the electrode performance via both TM and O redox.

Supporting Information

Supporting Information is available from the Wiley Online Library or from the author.

Acknowledgements

Conflict of Interest

The authors declare no conflict of interest.

Data Availability Statement

The data that support the findings of this study are available on request from the corresponding author. The data are not publicly available due to privacy or ethical restrictions.

Keywords

[1] J. Y. Hwang, S. T. Myung, Y. K. Sun, *Chem. Soc. Rev.* **2017**, *46*, 3529.

[2] C. Vaalma, D. Buchholz, M. Weil, S. Passerini, *Nat. Rev. Mater.* **2018**, *3*, 18013.

[3] K. M. Abraham, *ACS Energy Lett.* **2020**, *5*, 3544.

[4] L. F. Zhao, Z. Hu, W. H. Lai, Y. Tao, J. Peng, Z. C. Miao, Y. X. Wang, S. L. Chou, H. K. Liu, S. X. Dou, *Adv. Energy Mater.* **2021**, *11*, 2002704.

[5] C. H. Jo, N. Voronina, Y. K. Sun, S. T. Myung, *Adv. Mater.* **2021**, *33*, 2006019.

[6] S. Luo, T. Yuan, L. Soule, J. Ruan, Y. Zhao, D. Sun, J. Yang, M. Liu, S. Zheng, *Adv. Funct. Mater.* **2020**, *30*, 1908309.

[7] N. Voronina, J. H. Jo, J. U. Choi, A. Konarov, J. Kim, S. T. Myung, *J. Power Sources* **2020**, *455*, 227976.

[8] F. He, C. Tang, G. Zhu, Y. Liu, A. Du, Q. Zhang, *Sci. China Chem* **2021**, *64*, 964.

[9] A. Mendiboure, C. Delmas, P. Hagenmuller, *J. Solid State Chem.* **1985**, *57*, 323.

[10] X. Ma, H. Chen, G. Ceder, *J. Electrochem. Soc.* **2011**, *158*, A1307.

[11] N. Voronina, H. J. Kim, M. Shin, S. Myung, *J. Power Sources* **2021**, *514*, 230581.

[12] L. Zhang, T. Yuan, L. Soule, H. Sun, Y. Pang, J. Yang, S. Zheng, *ACS Appl. Energy Mater.* **2020**, *3*, 3770.

[13] N. Voronina, H. J. Kim, A. Konarov, N. Yaqoob, K. S. Lee, P. Kaghazchi, O. Guillon, S. T. Myung, *Adv. Energy Mater.* **2021**, *11*, 2003399.

[14] Z. Lu, J. R. Dahn, *J. Electrochem. Soc.* **2001**, *148*, A1225.

[15] A. Konarov, J. U. Choi, Z. Bakenov, S. T. Myung, *J. Mater. Chem. A* **2018**, *6*, 8558.

[16] N. Yabuuchi, M. Kajiyama, J. Iwatate, H. Nishikawa, S. Hitomi, R. Okuyama, R. Usui, Y. Yamada, S. Komaba, *Nat. Mater.* **2012**, *11*, 512.

[17] J. W. Somerville, A. Sobkowiak, N. Tapia-Ruiz, J. Billaud, J. G. Lozano, R. A. House, L. C. Gallington, T. Ericsson, L. Häggström, M. R. Roberts, U. Maitra, P. G. Bruce, *Energy Environ. Sci.* **2019**, *12*, 2223.

[18] W. Kang, Z. Zhang, P. K. Lee, T. W. Ng, W. Li, Y. Tang, W. Zhang, C. S. Lee, D. Y. Wai Yu, *J. Mater. Chem. A* **2015**, *3*, 22846.

[19] A. Konarov, H. J. Kim, N. Voronina, Z. Bakenov, S. T. Myung, *ACS Appl. Mater. Interfaces* **2019**, *11*, 28928.

[20] N. Voronina, M. Shin, H. Kim, N. Yaqoob, O. Guillon, S. H. Song, H. Kim, H. Lim, H. Jung, Y. Kim, H. Lee, K. Lee, K. Yazawa, K. Gotoh, P. Kaghazchi, S. Myung, *Adv. Energy Mater.* **2022**, *12*, 2103939.

[21] X. Rong, E. Hu, Y. Lu, F. Meng, C. Zhao, X. Wang, Q. Zhang, X. Yu, L. Gu, Y. S. Hu, H. Li, X. Huang, X. Q. Yang, C. Delmas, L. Chen, *Joule* **2019**, *3*, 503.

[22] R. A. House, U. Maitra, M. A. Pérez-Osorio, J. G. Lozano, L. Jin, J. W. Somerville, L. C. Duda, A. Nag, A. Walters, K. J. Zhou, M. R. Roberts, P. G. Bruce, *Nature* **2020**, *577*, 502.

[23] R. J. Clément, J. Billaud, A. R. Armstrong, G. Singh, T. Rojo, P. G. Bruce, C. P. Grey, *Energy Environ. Sci.* **2016**, *9*, 3240.

[24] E. N. Bassey, P. J. Reeves, M. A. Jones, J. Lee, I. D. Seymour, G. Cibin, C. P. Grey, *Chem. Mater.* **2021**, *33*, 4890.

[25] E. Boivin, R. A. House, M. A. Pérez-Osorio, J. J. Marie, U. Maitra, G. J. Rees, P. G. Bruce, *Joule* **2021**, *5*, 1267.

[26] A. Konarov, J. H. Jo, J. U. Choi, Z. Bakenov, H. Yashiro, J. Kim, S. T. Myung, *Nano Energy* **2019**, *59*, 197.

[27] X. Bai, M. Sathiya, B. Mendoza-Sánchez, A. Iadecola, J. Vergnet, R. Dedryvère, M. Saubanère, A. M. Abakumov, P. Rozier, J. M. Tarascon, *Adv. Energy Mater.* **2018**, *8*, 1802379.

[28] B. Song, M. Tang, E. Hu, O. J. Borkiewicz, K. M. Wiaderek, Y. Zhang, N. D. Phillip, X. Liu, Z. Shadike, C. Li, L. Song, Y. Y. Hu,

[29] M. Chi, G. M. Veith, X. Q. Yang, J. Liu, J. Nanda, K. Page, A. Huq, *Chem. Mater.* **2019**, *31*, 3756.

[29] Y. Li, X. Wang, Y. Gao, Q. Zhang, G. Tan, Q. Kong, S. Bak, G. Lu, X. Q. Yang, L. Gu, J. Lu, K. Amine, Z. Wang, L. Chen, *Adv. Energy Mater.* **2019**, *9*, 1803087.

[30] S. J. Park, J. Lee, I. H. Ko, S. Koo, S. H. Song, C. Koo, G. H. Yoon, T. Y. Jeon, H. Kim, D. Kim, S. H. Yu, *Energy Storage Mater.* **2021**, *42*, 97.

[31] N. Tapia-Ruiz, W. M. Dose, N. Sharma, H. Chen, J. Heath, J. W. Somerville, U. Maitra, M. S. Islam, P. G. Bruce, *Energy Environ. Sci.* **2018**, *11*, 1470.

[32] A. Konarov, H. J. Kim, J. H. Jo, N. Voronina, Y. Lee, Z. Bakenov, J. Kim, S. T. Myung, *Adv. Energy Mater.* **2020**, *10*, 2001111.

[33] H. J. Kim, A. Konarov, J. H. Jo, J. U. Choi, K. Ihm, H. K. Lee, J. Kim, S. T. Myung, *Adv. Energy Mater.* **2019**, *9*, 1901181.

[34] N. Yabuuchi, R. Hara, M. Kajiyama, K. Kubota, T. Ishigaki, A. Hoshikawa, S. Komaba, *Adv. Energy Mater.* **2014**, *4*, 1301453.

[35] E. De La Llave, E. Talaie, E. Levi, P. K. Nayak, M. Dixit, P. T. Rao, P. Hartmann, F. Chesneau, D. T. Major, M. Greenstein, D. Aurbach, L. F. Nazar, *Chem. Mater.* **2016**, *28*, 9064.

[36] C. Zhao, C. Li, H. Liu, Q. Qiu, F. Geng, M. Shen, W. Tong, J. Li, B. Hu, *J. Am. Chem. Soc.* **2021**, *143*, 18652.

[37] C. Li, C. Zhao, B. Hu, W. Tong, M. Shen, B. Hu, *Chem. Mater.* **2020**, *32*, 1054.

[38] C. Zhao, Q. Yang, F. Geng, C. Li, N. Zhang, J. Ma, W. Tong, B. Hu, *ACS Appl. Mater. Interfaces* **2021**, *13*, 360.

[39] M. Tang, A. Dalzini, X. Li, X. Feng, P. H. Chien, L. Song, Y. Y. Hu, *J. Phys. Chem. Lett.* **2017**, *8*, 4009.

[40] R. J. Clément, J. Xu, D. S. Middlemiss, J. Alvarado, C. Ma, Y. S. Meng, C. P. Grey, *J. Mater. Chem. A* **2017**, *5*, 4129.